



Deliverable 3.2.

Material resistance of combustor and turbine components, report on testing



Document control sheet

Project	Fit4Micro
Grant Agreement n°	101083536
Coordinator	Michel Delanaye
Work Package n°	3
Work Package title	Flameless combustion for liquid fuels development and high temperature material assessment
Work Package leader	OWI
Deliverable	3.2
Title	Material resistance of combustor and turbine components, report on testing
Version	1
Lead Beneficiary	MITIS
Author	Siri Harboe-Minwegen
Reference period	Second Period
Due date	M24
Submission date	
Dissemination level	Public



Table of Contents

1.	Introduction	6
2.	Experimental	6
2.1.	Materials.....	6
2.2.	Methods	8
2.2.1.	Creep Tests	8
2.2.2.	Analysis model for stress and strain	10
2.2.3.	Corrosion Tests	14
3.	Results.....	16
3.1.	Creep test results.....	16
3.2.	Corrosion test results	20
4.	Conclusion and outlook	23

List of Pictures

Figure 1:	Samples of Experiment 2 in the test furnace before starting the creep bending test.	8
Figure 2:	Larson Miller plot for Inconel 718.....	9
Figure 3:	Force diagram of cantilever beam with weight.	11
Figure 4:	Bending normal stress along beam thickness.....	11
Figure 5:	Example of tensile stress at $w=c$ over the length of the beam.....	12
Figure 6:	Centre line of the beam at time $t = 0$ (left) and a time $t > 0$ (right).	12
Figure 7:	Circle of curvature to the curve of the centre line of the beam at x	13
Figure 8:	Principal sketch of curved beam.....	13
Figure 9:	Determination of the centre line of the bars. From the measured values (y - coordinate).....	14
Figure 10:	Principal sketch of the tube furnace (above). Sample holder and positioning of samples (below).	15
Figure 11:	Experiment 2 creep bending samples after 100h at 900°C.	16
Figure 12:	Bending deflection of creep bending test samples of material SS310S.	17
Figure 13:	Bending deflection of creep bending test samples of material SS347.	18
Figure 14:	Bending deflection of creep bending test samples of material INCONEL 718.	18
Figure 15:	Strain versus time for various stresses and temperatures for SS310S	19
Figure 16:	Strain versus time for various stresses and temperatures for SS347	19
Figure 17:	Strain versus time for various stresses and temperatures for INCONEL 718	20
Figure 18:	Mass change versus time for the alloys in combust gas (without additional humidification) at temperatures 650, 700 and 750°C.....	21
Figure 19:	Photographs of the samples after 270 h exposure at 650°C in combust gas.	21
Figure 20:	Mass change versus time for the alloys in combust gas (with additional humidification) at temperatures 650°C and 1000h.....	22



Figure 21: Photographs of the samples after 305 h exposure at 650°C in combust gas with additional humidification..... 22

List of Tables

Table 1: Typical Chemical Compositions of Selected Alloys 7
Table 2: Experimental matrix for creep test analyses 10
Table 3: Gas composition during testing. 15
Table 4: Experimental matrix of corrosion test conditions. 16



1. Introduction

The design and development of a micro gas turbine (MGT) system, including its heat exchanger and combustion chamber, for operation with biomass-derived liquid fuels necessitates careful consideration of material degradation phenomena. The operational lifespan of metallic components in such environments is often influenced by a complex interplay of corrosion, creep, and fatigue mechanisms. Moreover, the chemical composition of biomass-based fuels can result in corrosive flue gas atmospheres, and cycle humidification may further intensify corrosion processes under high-temperature conditions.

High-temperature alloys represent a significant portion of the system's capital expenditure (CAPEX), due to their high cost. Therefore, the selection of cost-effective materials is crucial for ensuring the economic viability of the MGT system. At the same time, the materials used in energy systems such as the MGT must meet demanding lifetime expectations.

Early in the project, it became clear that the heat exchanger is one of the main cost drivers of the system, partly due to the quantity of material required. As such, corrosion testing efforts were primarily focused on candidate materials for the heat exchanger. To improve energy efficiency and reduce costs, minimizing the wall thickness of the heat exchanger is desirable. However, thinner walls are more susceptible to aging and degradation via corrosion, further justifying the need for robust corrosion testing in this component.

Other critical components in terms of material degradation are the rotor shaft and tie-bolt (max temperature of 700°C), combustion chamber outer skin (max temperature of 1000°C) or heat exchanger enclosure skin (max temperature of 700°C). These are more massive components or thicker sheets, compared with thin sheets inside the heat exchanger. They are more vulnerable to long-term creep and fatigue rather than corrosion. Accordingly, creep testing efforts were concentrated on materials intended for components. Unfortunately, no bulk specimen of either Mar M246 or Mar M247 could be supplied for creep testing relevant for the turbine wheel application.

Based on a preselection of promising material candidates, a comprehensive test campaign was conducted to evaluate their performance under conditions representative of actual MGT operation - including high temperatures, corrosive combustion gases, and mechanical loads. The objective of these investigations was to identify materials capable of ensuring long-term durability and minimizing the risk of premature failure or rapid degradation. The findings of these tests are presented and discussed in this deliverable.

2. Experimental

2.1. Materials

For material selection, a multi-criteria approach was adopted. Considerations included technical performance, cost, and availability. All tested materials were commercially available ("off the shelf") from different standard suppliers in order to minimize potential bottleneck in availability. Both high-performance, proven alloys and more economical, lower-grade materials with uncertain long-term suitability were tested and benchmarked against each other. This enables an informed material selection process that balances durability and cost-efficiency, paving the way for optimized manufacturing of the MGT system.

The materials selected for system development and testing are as follows:



- Heat exchanger (corrosion testing): Inconel 800H, Stainless Steels (SS) 304, 310SS, 316, 321, 347
- Shaft / tie bolt, combustion chamber skin, HEX enclosure skin (creep testing): SS310S, 347, Inconel 718

The chemical compositions of these materials are provided in Table 1.

Table 1: Typical Chemical Compositions of Selected Alloys

Material	Fe (%)	Cr (%)	Ni (%)	C (%)	Mo (%)	Mn (%)	Si (%)	Nb/Ti/Others (%)
Inconel 800H [1]	Balance	19.0–23.0	30.0–35.0	0.05–0.10	—	≤1.5	≤1.0	Al: 0.15–0.60, Ti: 0.15–0.60
SS 304 [2]	Balance	17.5–19.5	8.0–10.5	0.07	—	2.0	1.0	—
SS 310S [3]	Balance	24.0–26.0	19.0–22.0	0.08	—	2.0	1.5	—
SS 316 [4]	Balance	16.0–18.0	10.0–14.0	≤0.08	2.0–3.0	≤2.0	≤1.0	—
SS 321 [5]	Balance	17.0–19.0	9.0–12.0	≤0.08	—	≤2.0	≤1.0	Ti: ≥5×C and ≤0.70
SS 347 [6]	Balance	17.0–19.0	9.0–12.0	0.08	—	2.0	1.0	Nb: ≥10×C and ≤1.0
Inconel 718 [7]	Balance	17.0–21.0	50.0–55.0	≤0.08	2.8–3.3	≤0.35	≤0.35	Nb: 4.75–5.5, Ti: 0.65–1.15, Al: 0.2–0.8
Material	Max Service Temp (°C)	Common applications	Notes	Material manufacturing and treatments				
Inconel 800H [1]	1100	Heat exchangers, furnaces, petrochemical	Excellent high-temp strength, oxidation resistant	Cold rolled, solution annealed, bright, slit edge				
SS 304 [2]	870 (continuous ~500)	Food industry, piping, kitchenware	Good corrosion resistance, limited high-temp use	EAF, Solution annealed, forced air/water				
SS 310S [3]	1100	Furnace parts, kilns, radiant tubes	High-temp oxidation resistance	Cold Rolled Sheet, Slit edge				
SS 316 [4]	870 (continuous ~500)	Chemical/marine equipment, heat exchangers	Mo improves pitting resistance	EAF, Solution annealed, forced air/water				
SS 321 [5]	900–925	Aircraft exhaust, expansion joints	Ti stabilized, intergranular corrosion resistant					
SS 347 [6]	870–925	Chemical processing, aerospace	Nb stabilized, creep resistance	Electric induction furnace, argon oxygen decarburization, continuous casting				



Inconel 718 [7]	650–700	Jet engines, turbines, cryogenics	High strength, weldable, corrosion resistant	Bar steel, rolled, solution annealed, age hardened
-----------------	---------	-----------------------------------	--	--

2.2. Methods

In the testing campaign, creep tests and corrosion tests were conducted separately using two different test apparatuses. The details of the testing methods are described in the following subchapters.

2.2.1. Creep Tests

Creep behavior of metallic bar samples was investigated using a chamber furnace at temperatures up to 1000 °C. The test setup (Figure 1) involved cantilever-mounted bending samples with dog-bone geometry bars clamped at one end, allowing them to deform under their own weight. These samples experience both tensile and compressive stresses in a cantilever beam stress distribution. Due to the direct comparison of the four specimens, this test setup minimizes measurement uncertainties typically associated with reproducibility issues which is a particularly challenging and costly aspect in long-term experiments. A dummy specimen was placed in the central position of the specimen holder for temperature monitoring, in the Figure 1 the fixation of 3 thermocouples with ceramic glue can be seen. The temperature distribution along its length was continuously recorded.



Figure 1: Samples of Experiment 2 in the test furnace before starting the creep bending test.

The experimental matrix was provisionally established by Mitis using the Larsen-Miller parameter (LMP) approach (considering creep life up to 1% creep strain) applied as post processing of analytical and finite element simulations of the creep bending tests, in order to achieve well spread LMP values, respecting the

secondary creep zone assumption, and allowing to confront with literature data obtained with tensile creep tests, when available. The methodology is presented below.

The Larson-Miller parameter approach starts from the following expression of the temperature (T) and stress (σ) activated visco-plastic creep strain

$$\dot{\epsilon} = Ae^{\left(\frac{\sigma\Omega - Q}{RT}\right)}$$

where A is a constant, Ω is the stress activation volume, Q is the thermal activation energy.

The essential assumption of the approach is that lifetime t_r up to a certain creep strain or up to creep failure is dictated by the minimum value of the secondary creep rate and that

$$t_r \cdot \dot{\epsilon}_{min} = C$$

where C is a constant.

Posing that $LMP = T(\log(t_r) + C)$, experimental results are usually plotted as stress values against LMP values, where the abscissa axis embeds the time-temperature equivalence, as shown hereafter for literature data on Inconel 718.

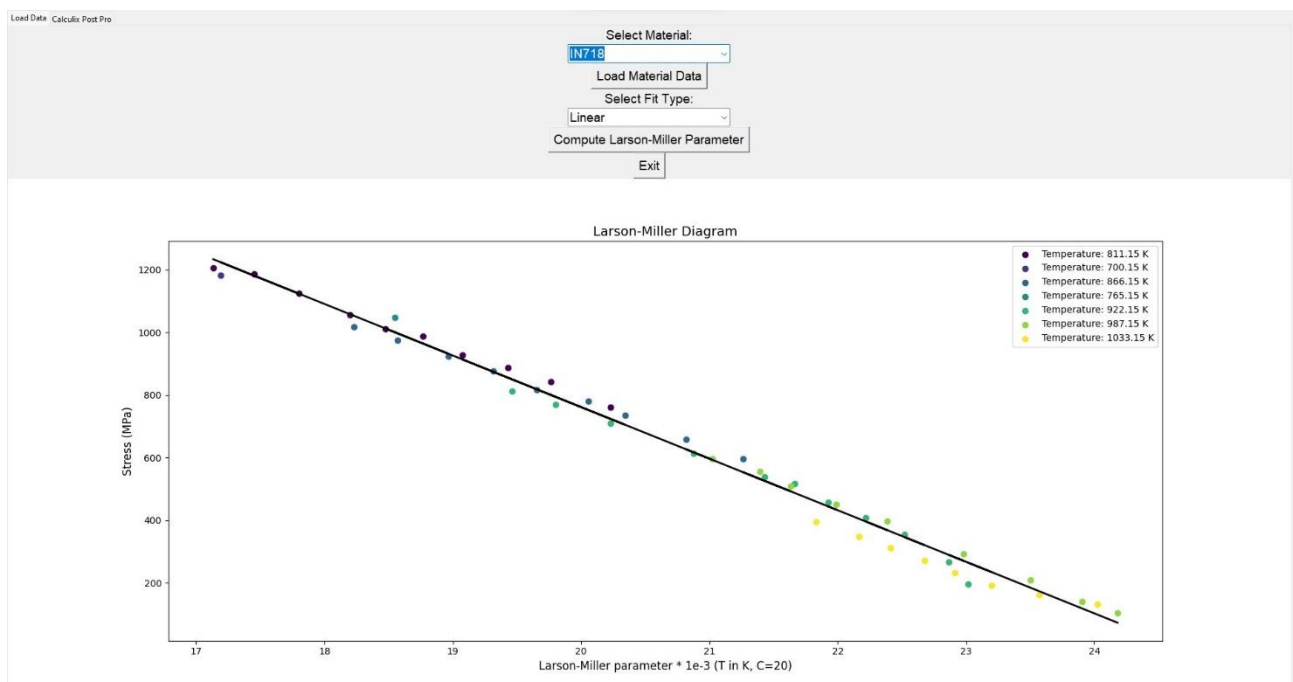


Figure 2: Larson Miller plot for Inconel 718.

In Figure 2, for instance, low LMP corresponds either to low time & large temperature or large time & low temperature, for a given stress. The data plotted in Figure 2 come from uniaxial tensile creep test, with a uniform stress across the test specimen section whereas in bending creep tests the stress is not uniform across the section. The rationale to determine the temperature, time, stress combination for bending test specimen is the following:

- Set the targeted creep strain (here 1%) at the outer surface of the bending specimen where the strains will be the largest.
- Set the maximum creep time allowable (here 100h)
- Define (bending load, temperature) couples so that the maximum section stress and LMP parameters are well spread across the known LMP plot for the considered material.

The final DoE was released by OWI to better match available creep loads, equipment availability, and somewhat adapted based on preliminary results.

Additionally, the materials were tested according to their expected operational limits. An overview of the experiments is presented in Table 2. For each experimental condition the experiment was repeated with two samples. For all the experiment the duration was 100h. The length of the samples was 190 mm. Due to machining tolerances the diameters were slightly differing from the aimed values (6.5 and 8 mm), as given in the Table 2. The determination of the stresses is described in the subchapter 2.2.2.

Table 2: Experimental matrix for creep test analyses

Exp.#	Samples	Material	diameter (mm)	T(°C)	Weight (g)	σ_{max} 0-50mm (MPa), Part1	σ_{max} 50-125mm (MPa) Part 2
1	1_1 and 1_3	SS347	7.7	800	360	15.8-10.4	10.4-2.7
	1_2 and 1_4	SS310S	7.7	800	2420	80.9-52.8	52.8-12
2	2_1 and 2_2	SS310S	7.7	900	1550	53.4-34.9	34.9-8.1
	2_3 and 2_4	INCO718	7.6	900	360	16.4-10.6	10.6-2.8
3	3_1 and 3_2	SS310S	7.2 + (7.5)	1000	100	9.2-6.0 (8.2-5.4)	6.0-1.9 (5.4-1.6)
	3_3 and 3_4	SS310S	7.5 + (8)	1000	650	27.0-17.7 (22.3-14.6)	17.7-4.3 (14.6 -3.6)
4	4_1 and 4_2	SS347	8	750	360	14.2- 9.3	9.3 - 2.4
	4_3 and 4_4	INCO718	6.6	750	2420	134-88	88-20
5	5_1 and 5_2	SS347	8	700	1120	35.6-23.2	23.2-5.5
	5_3 and 5_4	SS347	8	700	680	23.2-15.1	15.1-3.7
6	6_1 and 6_2	INCO718	6.6	800	2430	128.6-84.1	84.1-19.1
	6_3 and 6_4	SS310S	8	800	680	23.2-15.1	15.1-3.7

2.2.2. Analysis model for stress and strain

The analysis of creep properties was performed with a cantilever beam model, from which the stresses and strains were deduced. The analysis model applied in bending tests has been validated and compared with uniaxial tensile creep tests in previous study [8], and has for the current test apparatus previously been reported [9], and detailed described in the German national IGF project “Flexible Furnace Operation”, the report from which is present with Research Association of Industrial Furnace Manufactures, FOGI e. V. The force diagram of the cantilever beam is shown in Figure 3, with self-weight distributed loads w1, w2 and weight force, f3.

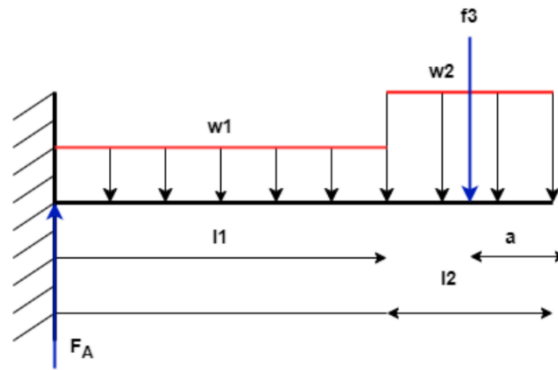


Figure 3: Force diagram of cantilever beam with weight.

Applying the Bernoulli beam theory, the bending momentum and stresses were determined, assuming that shear force stresses are negligible in comparison to bending moment stresses, as typically assumed for slim, long beams, and that stress concentrations occur at the surfaces, meaning that the maximum stress in the beam is at the surface. As in Bernoulli's beam theory, it is assumed that planes perpendicular to the centre line do not deform. Furthermore, that the bending normal stress $\sigma(x, t, w)$ depends linearly on the distance, w , to the centre line and that is equal to zero in the middle of the cylindrical beam (Figure 4).

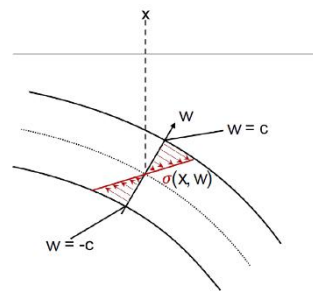


Figure 4: Bending normal stress along beam thickness.

This distribution of the bending stress results in the bending moment in the point x at the course of the of the beam given by

$$M(x, t) = \frac{\sigma(x, t, w)}{w} I \tag{Equation 1}$$

where I is the moment of inertia of the beam and $M(x, t)$ is the moment due to the self-weight of the beam and the weight attached to the end of the beam during the experiment. From the momentum equilibria, the normal stresses $\sigma(x, t, w)$ for the load situations are calculated for the sample geometries and added weights given in Table 2. The tensile stresses are positive due to sign convention. In Figure 5, tensile stress at $w=c$ over the length of the beam calculated for Exp. 1: beam length 204mm, weight 2420g, slim beam diameter 7.7mm, point of weight attachment 144 mm is shown as an example.

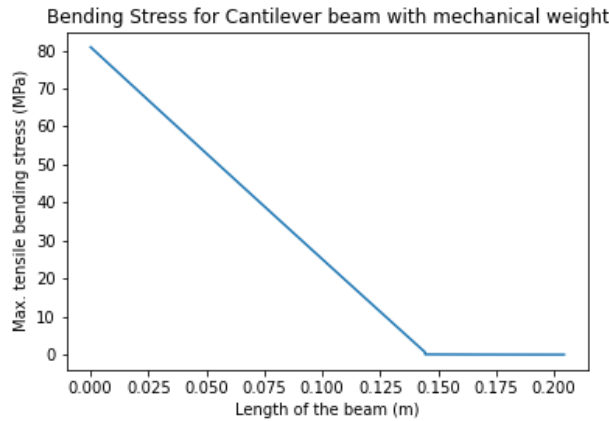


Figure 5: Example of tensile stress at w=c over the length of the beam.

As the beam bends downward due to creep, a tangential force component to the beam axis is present. This results in a tensile stress in this direction, which ultimately leads to an extension of the beam. As the maximum bending stress decreases, this tensile stress increases.

Determination of strain: In the strain analysis a geometric model is used where the course of the centre line of the bar at time t is given by the function f(x, t), where x is the position in the direction of the axis of the beam and y = f(x, t), see Figure 6.

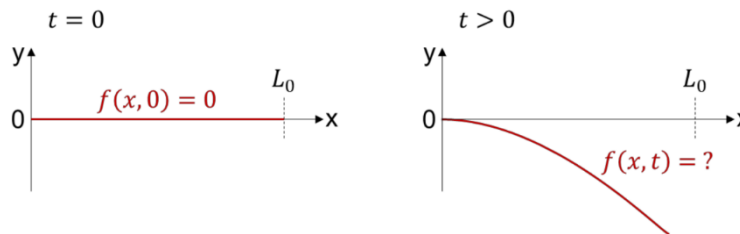


Figure 6: Centre line of the beam at time t=0 (left) and a time t>0 (right).

The beam is not deformed at time t = 0, i.e., the strain is $\epsilon(x,0) = 0$, for x between 0 and L0 where L0 is the specified initial length of the bar. At time t, the centre line f(x, t) at x has the curvature $\kappa(x, t)$, given by the geometric relationship:

$$\kappa(x, t) = \frac{1}{R(x, t)} = \frac{f''(x, t)}{(1 + f'(x, t)^2)^{3/2}} \tag{Equation 2}$$

Shown schematically in Figure 7:

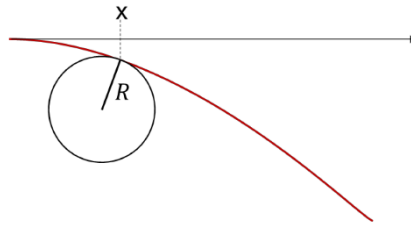


Figure 7: Circle of curvature to the curve of the centre line of the beam at x.

The expression for the beam deformation depending on the elongation dL is shown in Figure 8.

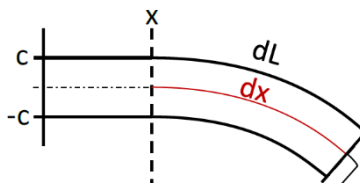


Figure 8: Principal sketch of curved beam.

The beam has the height $2c$. It is assumed that the length element dx of the centre line does not change its length compared to the initial state. Under the assumptions underlying Bernoulli's beam theory, the tension in the axial direction along the centreline is negligible. However, the top and bottom edges of the beam stretch and changes its length. The initial state applies to the upper edge $dL = dx$. When bent, the upper edge is stretched by ϵ . This leads to the equation:

$$dL = dx(1 + \epsilon) \tag{Equation 3}$$

Using the intercept theorem, one obtains the following relationship between the lengths dL and dx and the radius of the circle of curvature applied to position x .

$$\frac{dx}{R} = \frac{dL}{R + c} \tag{Equation 4}$$

and overall, after substituting dL from equation Equation 3 into Equation 4:

$$\kappa(x, t) = \frac{1}{R(x, t)} = \frac{\epsilon(x, t)}{c} \tag{Equation 5}$$

Determination of function $f(x,t)$: The function was determined by regression fit of experimental data. For each beam sample, the y -coordinates were recorded before and after exposure in the experiment. Top edge of beam measured (Figure 9 a) to b)). These values became the centre line of the bar was determined locally as follows: First, the measured values were considered. A second-degree polynomial $f(x)_{OK}$ was generated in the area using regression, which reflects the shape of the upper edge in the area under consideration (Figure 9 b) to c)). Out of function $f(x)_{OK}$, the function $f(x)$ of the centreline was calculated by pointing to each point of $f(x)_{OK}$. Normal vector with length of half the beam thickness was added (Figure 9 c) to d)). The representative strains were evaluated in two sections of the slim beam, 0-50 mm and 50-125 mm, respectively, corresponding to stresses σ_{max} 0-50mm and σ_{max} 50-125mm in Table 2.

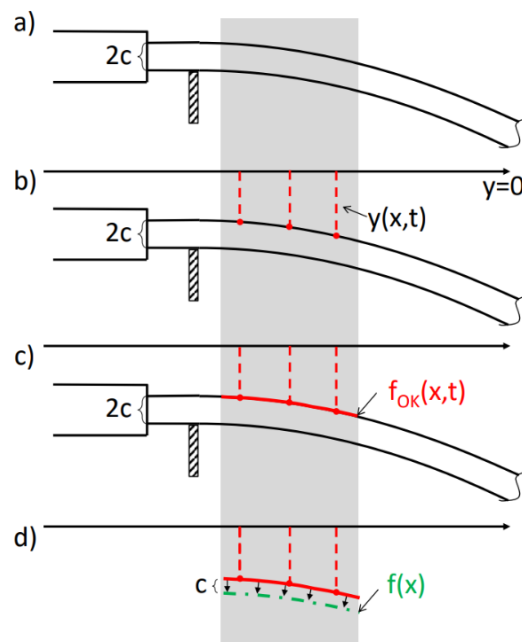


Figure 9: Determination of the centre line of the bars. From the measured values (y -coordinate).

2.2.3. Corrosion Tests

At OWI, long-term corrosion tests were conducted in a tube furnace capable of simulating various flue gas atmospheres at temperatures up to 1050 °C. To replicate the operational conditions of the heat exchanger, tests were performed in the 650–750 °C range, which is also critical for material stability due to possible formation of brittle intermetallic phases.

System simulations provided by project partners (Mitis) informed the selection of flue gas compositions and temperature settings, which correspond to steady-state operating conditions on the hot side of the heat exchanger. Gas atmospheres were generated either by combustion of natural gas, diesel, or biofuels using an integrated burner or by mixing bottled gases (CO₂, H₂O, O₂, N₂).

The gas compositions used during the tests are listed in Table 3. The selected composition simulates combustion of diesel or heating oil at an air ratio (λ) of 4—richer in CO₂ and H₂O than typical

operational conditions. This deliberately harsher atmosphere was chosen to accelerate corrosion and simulate material exposure during off-nominal conditions, such as start-stop cycles.

Additionally, some test runs included increased humidification to reflect moisture levels expected in humidified cycle operation, as predicted by system simulations. These were conducted to study the effect of water vapor on corrosion mechanisms. The humidification level was set corresponding to operation with adding 5g/s of water, at $\lambda = 4$ and 50kW power.

Table 3: Gas composition during testing.

Combustion	Gas atmosphere [vol.%]			
	CO ₂	N ₂	O ₂	H ₂ O
Heating oil /Air $\lambda = 4$, @650°C	3.6	77	15.5	3.2
Heating oil /Air $\lambda = 4$, @650°C + humidification	3.0	69.8	13.7	13.6

Test Procedure:

Samples from each material (two per material type) were laser cut and placed in the furnace (Figure 10). The samples were oxidized in air at the set-point temperature for 24 h, before the experiment with the gas compositions in question was started. The experimental conditions are shown in Table 4. The durations of each experiment were 500 and 1000h, respectively. The gas flow rate through the furnace was 7 slm. At regular intervals, the samples were removed, weighed, and photographed to assess mass loss and observe optical changes such as oxide layer flaking.

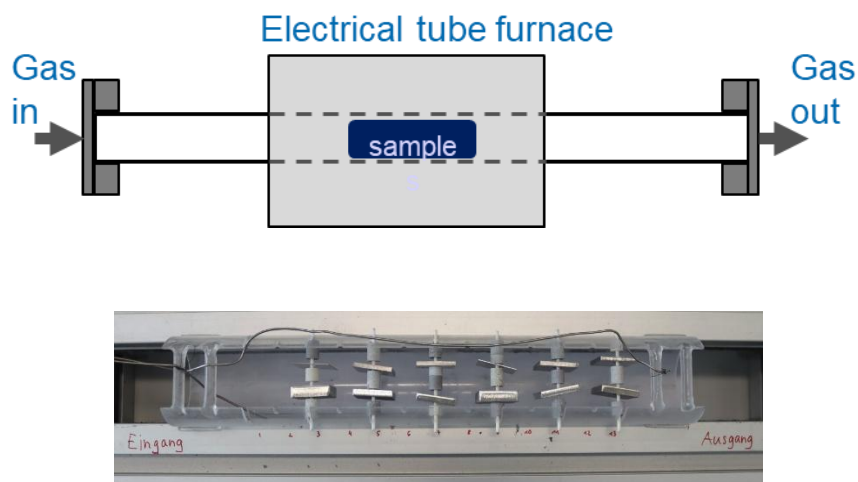


Figure 10: Principal sketch of the tube furnace (above). Sample holder and positioning of samples (below).

Table 4: Experimental matrix of corrosion test conditions.

Experiment #	Temperature, °C	Gas composition
1	650	Combust, Lambda4
2	650	Hum. combust gas, Lambda4
3	700	Combust, Lambda4
4	750	Combust, Lambda4

3. Results

3.1. Creep test results

The samples after the exposure in the test furnace show bending depending on the material, the temperature and mechanical load. An example to illustrate this is shown in Figure 11, experiment 2 conditions are given in Table 2.



Figure 11: Experiment 2 creep bending samples after 100h at 900°C.

The bending deflections for the material SS310S are shown in Figure 12 for different temperatures and mechanical stresses. In each graph, the results of the respective two repetitions in black and gray data points are shown with loading before (0h) and after (100h) exposure, displaying reproducibility of the experiments. The tested temperatures were 800, 900 and 1000°C and the stresses (maximum bending stress) between 9.2 and 80.9 MPa. As expected, the bending deflection increases with increasing stress and temperature.

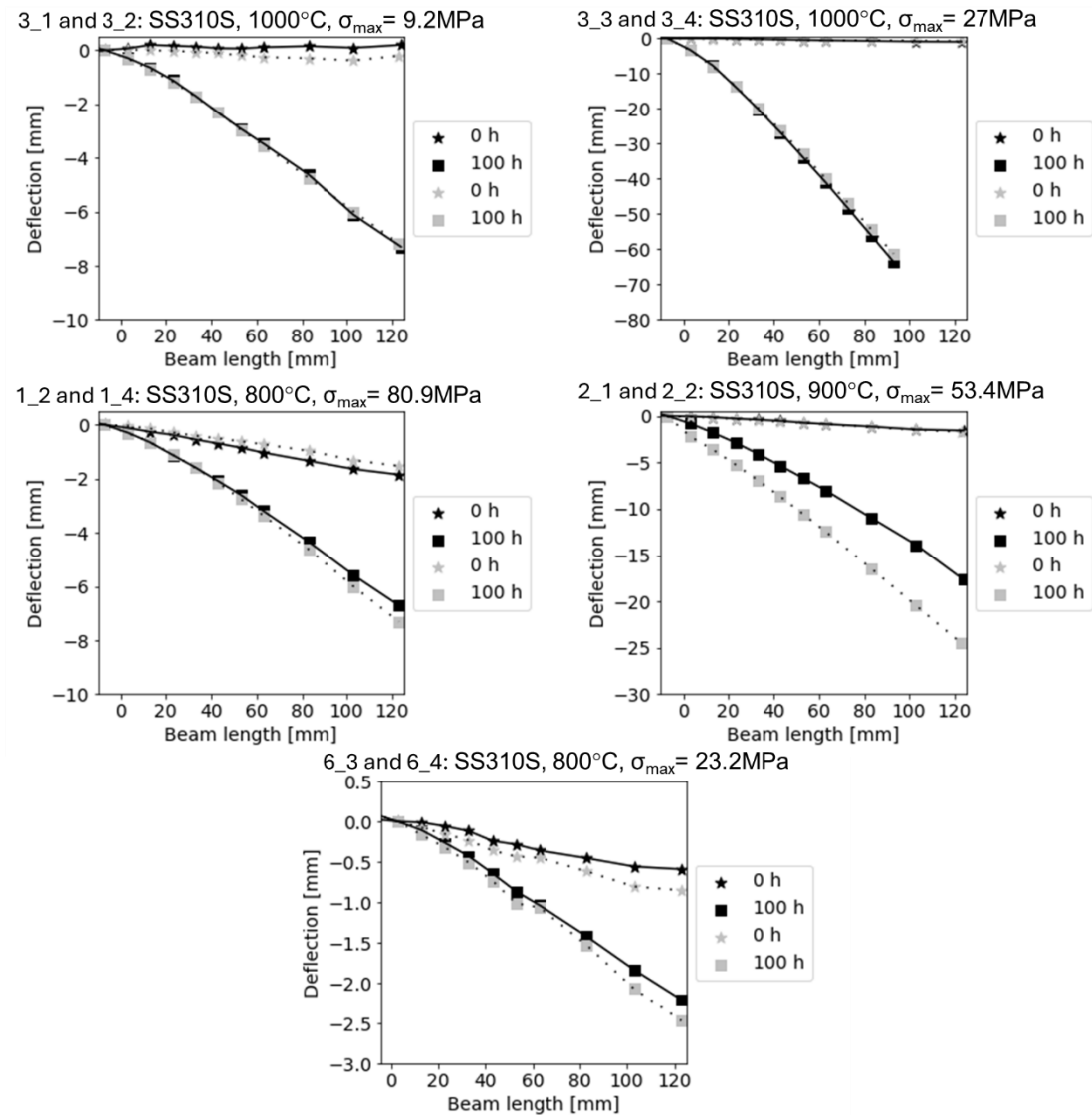


Figure 12: Bending deflection of creep bending test samples of material SS310S.

Similarly, the bending deflection for the material SS347 is shown in Figure 13 for temperatures 700-800°C and mechanical stresses 14.2-35.6MPa.

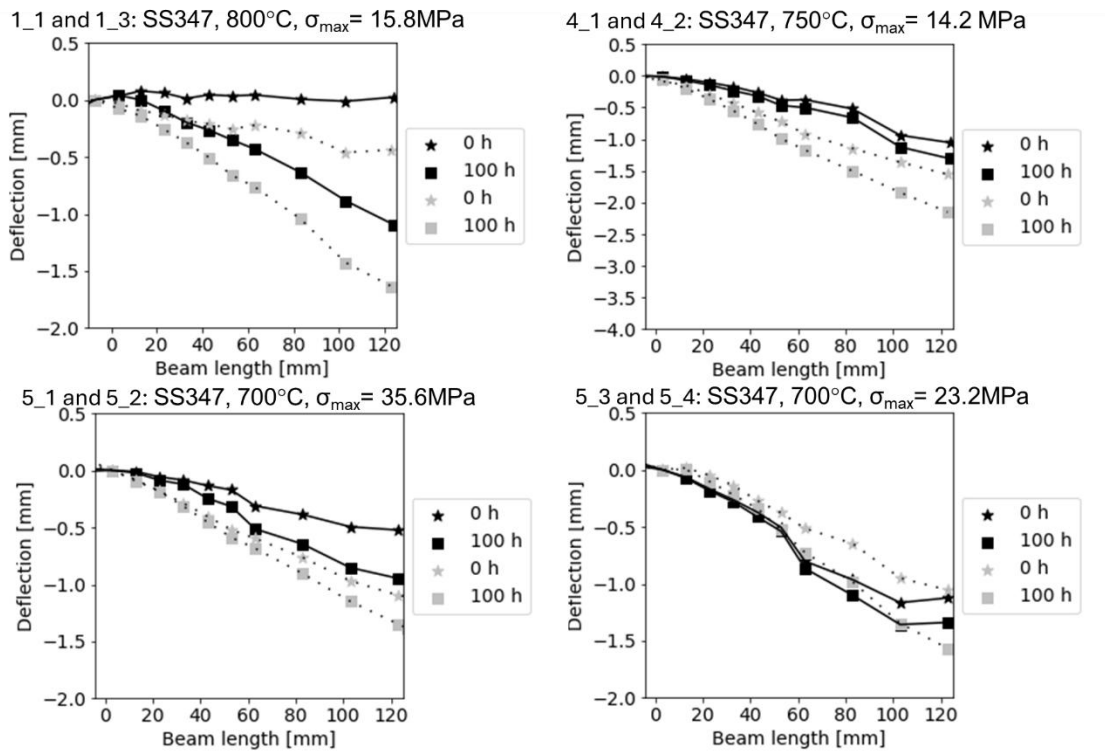


Figure 13: Bending deflection of creep bending test samples of material SS347.

Similarly, the bending deflection for the material INCONEL718 is shown in Figure 14 for temperature of 750-900°C and mechanical stresses/maximum bending stresses of 16.5-134 MPa.

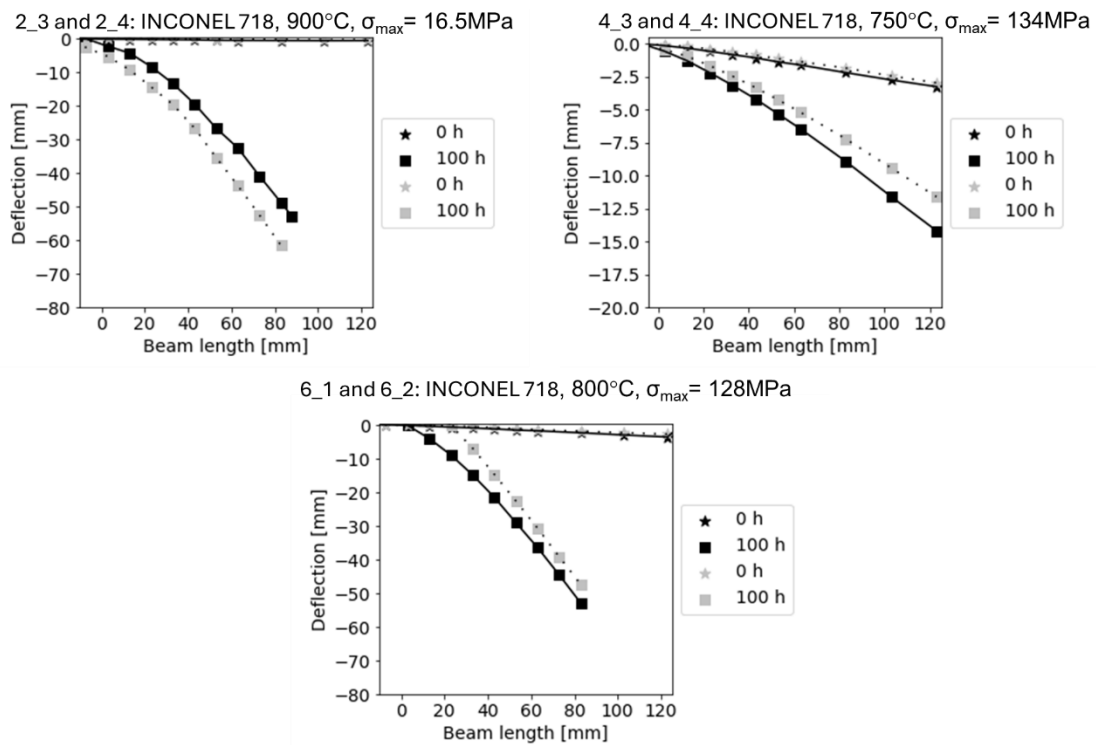


Figure 14: Bending deflection of creep bending test samples of material INCONEL 718.

Based on the bending deflection, the strains were determined using the method described in subchapter 2.2.2. The strain versus time curves for different temperatures and stress levels are shown for the material SS310S in Figure 15, SS347 in Figure 16 and INCONEL718 in Figure 17. The conditions applied to the samples are summarized in Table 2.

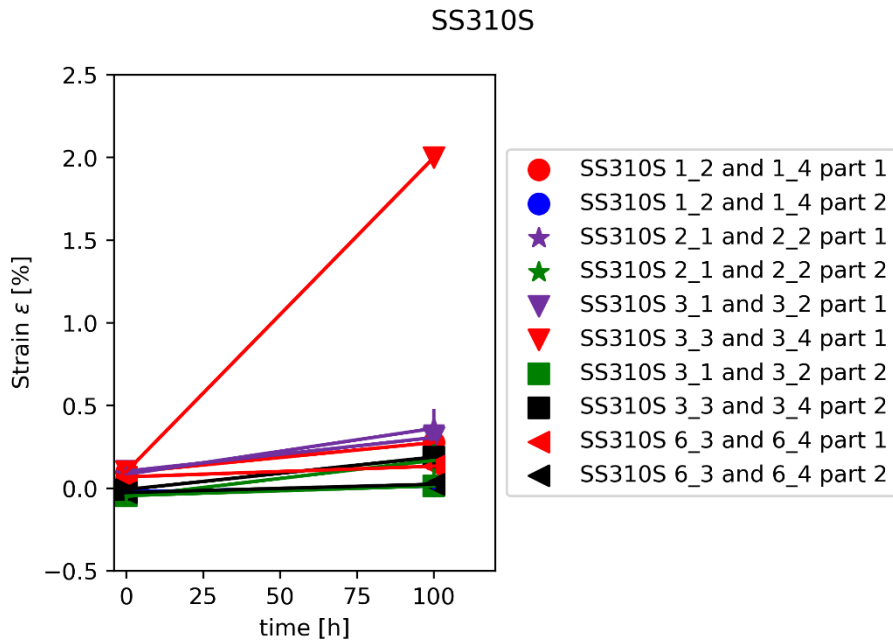


Figure 15: Strain versus time for various stresses and temperatures for SS310S

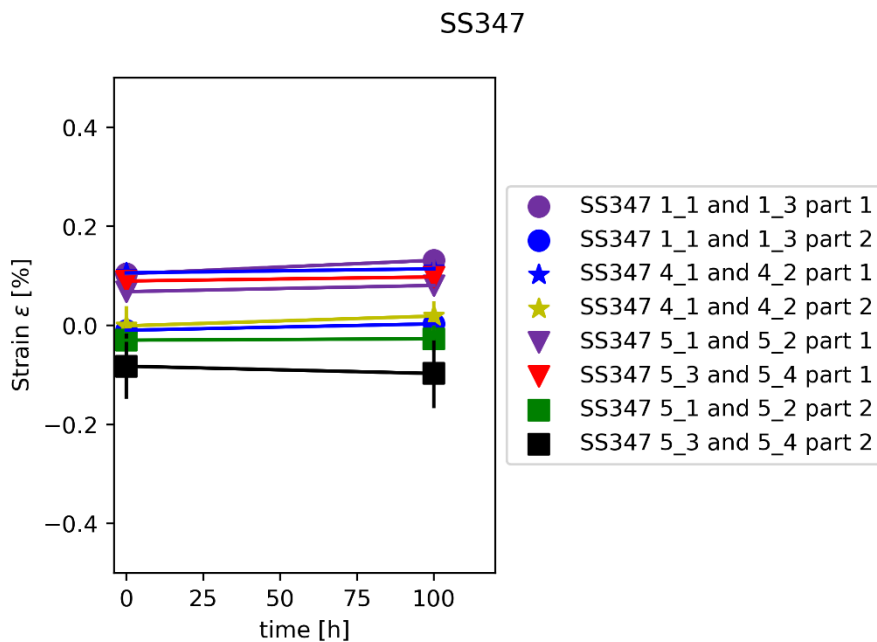


Figure 16: Strain versus time for various stresses and temperatures for SS347

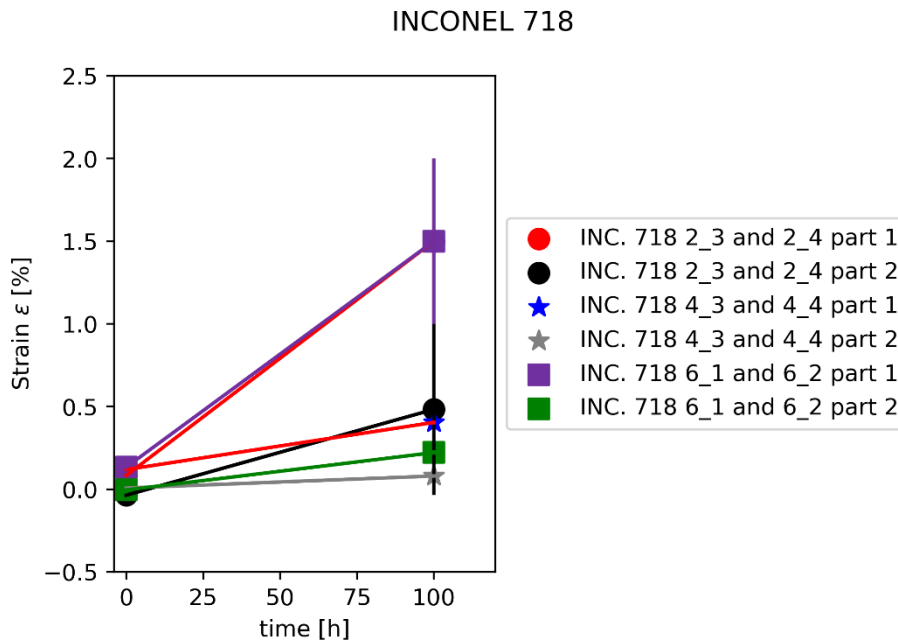


Figure 17: Strain versus time for various stresses and temperatures for INCONEL 718

As shown in Figure 12 the SS310S cannot withstand the temperature of 1000°C with the applied maximum bending stress of 27MPa and shows strains of 2%. In Figure 17 it can be observed that INCONEL 718 does not exhibit sufficient creep resistance at temperatures above 750 °C, specifically maximum bending stress 128 MPa at 800 °C and 16.4 MPa at 900 °C shows a significant creep rate of 1.6% after 100h duration. The stress and temperature testing conditions for SS347 were less severe, the material showed creep strains below 0.2%. Some of the strains were measured as negative. This is because the finishing tolerances of the samples cause curvature with samples bending upwards (see bending deflections in Figure 12, Figure 13 and Figure 14), which is then interpreted as negative strain.

3.2. Corrosion test results

Figure 18 presents the mass change over time for the tested materials at 650 °C, 700 °C, and 750 °C under combust gas conditions. The results show that, based on the weight change, alloy 800H exhibits the highest corrosion resistance, followed by SS310S, SS347/SS321 in descending order of performance. In contrast, SS304 and SS316 demonstrate irregular mass changes and notable mass losses, particularly at elevated temperatures (700 °C and 750 °C), suggesting accelerated oxide scale formation and spallation. Photographs of the samples after 270 h of exposure (Figure 19) further corroborate these findings, showing pronounced surface scaling on SS304 and SS316, even at intermediate temperatures. These visual observations align with the mass change data and indicate compromised oxidation resistance in these alloys under the test conditions.

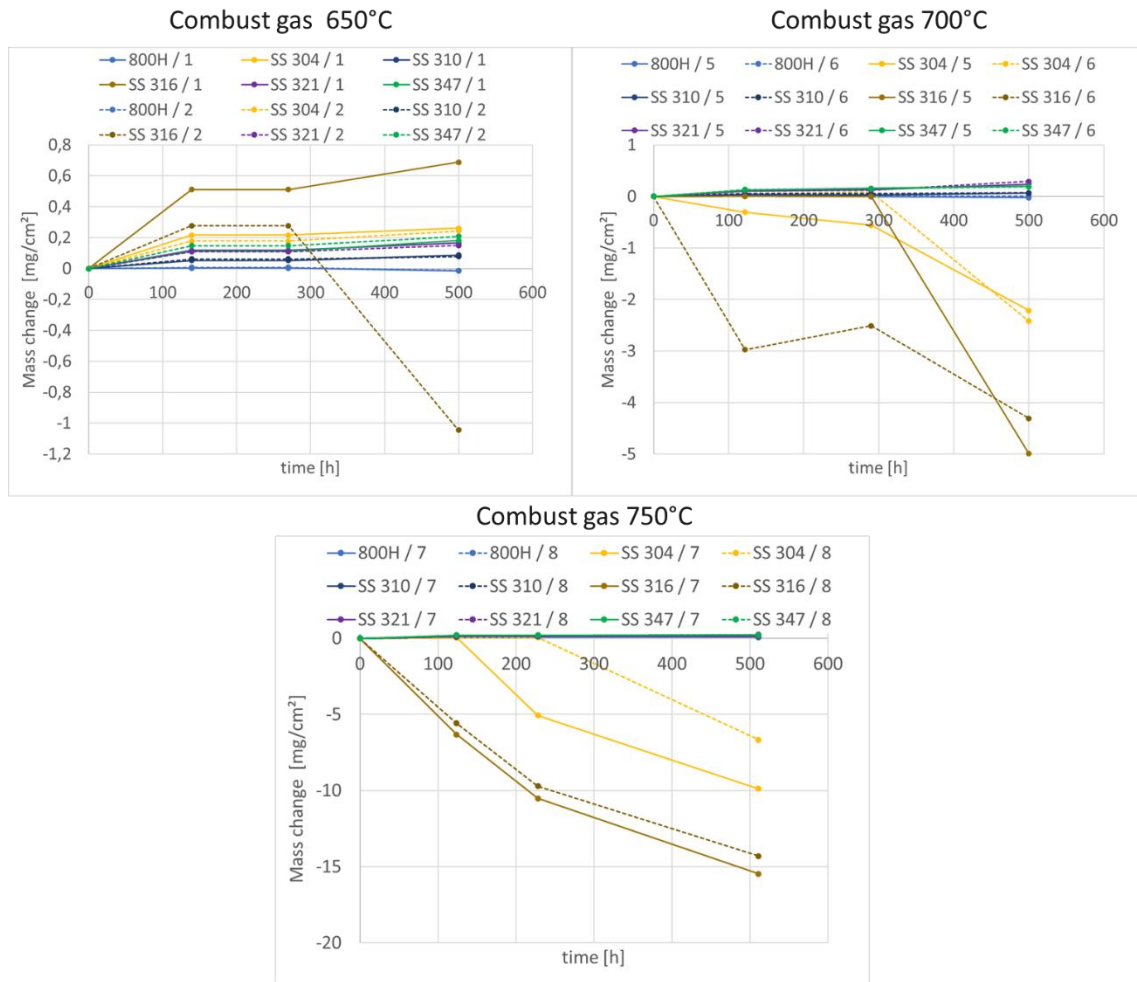


Figure 18: Mass change versus time for the alloys in combust gas (without additional humidification) at temperatures 650, 700 and 750°C.

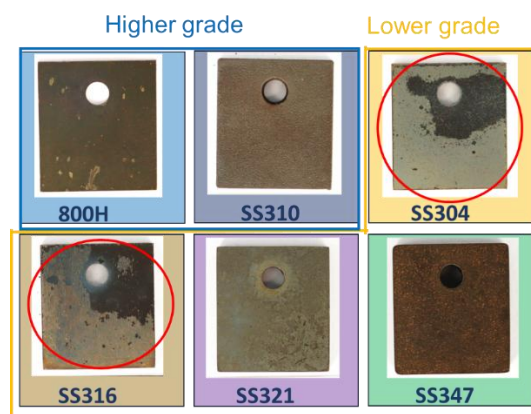


Figure 19: Photographs of the samples after 270 h exposure at 650°C in combust gas.

In Figure 20 the weight change over time for the samples under combust and additionally with cycle humidification at 650 °C. The results highlight alloy 800H as again exhibiting the highest corrosion resistance, followed by SS310S, SS347 in descending order of performance. The alloys SS304, SS316 and SS321 show irregular mass changes and notable mass losses suggesting accelerated oxide scale formation and spallation.

Photographs of the samples after 305h of exposure (Figure 21) are also showing pronounced surface scaling on SS316 and SS321 at 650°C. These visual observations align with the mass change data and indicate compromised oxidation resistance in these alloys under the test conditions, showing that the humidification especially had a negative effect on the alloy SS321 in comparison to the combust conditions without additional humidification.

At 650°C It was found that under combust conditions without additional humidification the mass change was lower than under combust conditions with additional humidification. Under the more humid conditions the mass change was mainly negative and under dry conditions the mass change was positive. At the same time considerable flaking was observed under more humid conditions.

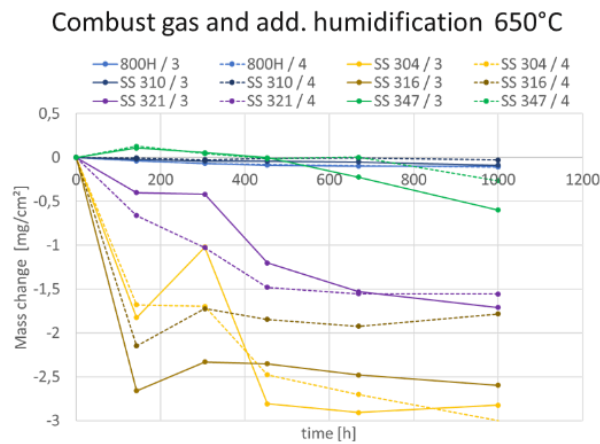


Figure 20: Mass change versus time for the alloys in combust gas (with additional humidification) at temperatures 650°C and 1000h.

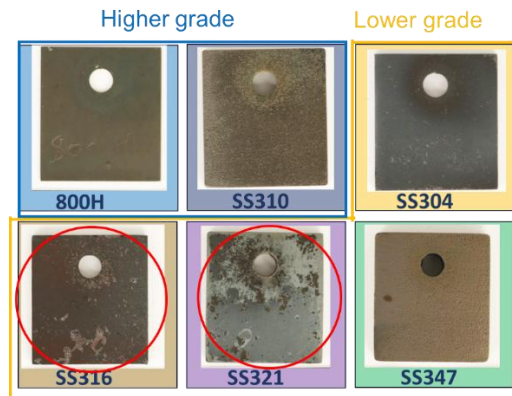


Figure 21: Photographs of the samples after 305 h exposure at 650°C in combust gas with additional humidification.

4. Conclusion and outlook

The materials were tested under conditions representative of the operational environment of the micro gas turbine. Two test campaigns were conducted: one focusing on creep behavior and the other on corrosion resistance.

Creep Testing:

SS347 and SS310S showed better creep resistance compared to INCONEL 718 at temperatures of 800 °C and above for the tested stress levels. Furthermore, the SS310S, showed significant creep at 1000°C for the tested stress conditions.

Corrosion Testing:

The higher-grade alloys 800H and SS310S consistently demonstrated the better corrosion resistance across all test conditions. Among the lower-grade materials, SS347 performed more reliably throughout the tested conditions than the other alloys. The distinguishing factor between SS321, SS347, SS304, and SS316 lies in their alloying elements (see Table 1): SS316 has a higher nickel content and contains molybdenum (Mo); SS321 is alloyed with titanium; SS347 includes niobium. These elements form stable carbides that bind carbon and prevent chromium carbide precipitation at grain boundaries—thereby reducing the risk of chromium depletion, intergranular corrosion, and embrittlement. It might be that Niobium alloying was giving the better performance of the alloy SS347. It remains unclear whether different surface treatments and cold rolling also may have contributed to the improved performance of SS347.

Outlook:

The creep tests results will be used by Mitis to generate (LMP, stress) couples that will be compared to LMP plots obtained with tensile creep tests. Furthermore, an elastic-viscoplastic model will be identified based on literature data and a subset of the bending creep tests results e.g. for Inconel 718. The elastic-viscoplastic modeling and elastic based LMP approach will be compared in terms of accuracy of creep deformation versus time to the light of the experimental bending deformation results. This will be presented in a subsequent publication.

Ongoing tests are currently exploring material corrosion behavior at elevated temperatures up to 750 °C, for combustion and additionally humidified environments. Due to time constraints of the current reporting period, these results will be presented in a subsequent scientific publication.

Literature

- [1] Special Metals, „Special Metals - Incoloy 800H Datasheet,“ [Online]. Available: <https://www.specialmetals.com/documents/technical-bulletins/incoloy/incoloy-alloy-800h-800ht.pdf>. [Zugriff am 16 Juni 2025].
- [2] Thyssenkrupp, „Stainless Steel 304 1.4301,“ [Online]. Available: <https://www.thyssenkrupp-materials.co.uk/stainless-steel-304-14301.html>. [Zugriff am 01 07 2025].



- [3] Super Metals, „SS310s,“ [Online]. Available: <https://super-metals.com/wp-content/uploads/2015/03/SS-310.pdf>. [Zugriff am 01 07 2025].
- [4] SJZ Metals in Tech Co Ltd, „SS316,“ [Online]. Available: <http://www.metalspiping.com/ss316-ss316l.html>. [Zugriff am 01 07 2025].
- [5] Thyssenkrupp, „SS321,“ [Online]. Available: <https://www.thyssenkrupp-materials.co.uk/stainless-steel-321-14541.html>. [Zugriff am 01 07 2025].
- [6] Thyssenkrupp, „SS347,“ [Online]. Available: <https://www.thyssenkrupp-materials.co.uk/stainless-steel-347-14550.html>. [Zugriff am 01 07 2025].
- [7] Special Metals, „Inconel 718,“ [Online]. Available: <https://www.specialmetals.com/documents/technical-bulletins/inconel/inconel-alloy-718.pdf>. [Zugriff am 01 07 2025].
- [8] H. Ackermann und P. Bittner, „Lebensdauer metallischer Ofenkomponenten bei Temperaturwechselbeanspruchung (Teil 2),“ *Prozesswärme*, Bd. 6, pp. 89-99, 2019.
- [9] S. Harboe-Minwegen, D. Kuckelberg, R. Schwing und E. Pohl, „Creep bending tests of alloys during superimposed thermal cycling,“ in *Proceedings of the 14th European Conference on Industrial Furnaces and Boilers (INFUB-14)*, 2-5 April 2024. Algarve, Portugal, 2024.
- [10] K. Raj, „ON HIGH TEMPERATURE MATERIALS: STRESS-RUPTURE CHARACTERISTICS OF AISI 310S STAINLESS STEEL SHEETS AT TEMPERATURE 973-1073K UNDER APPLIED STRESS 40-150MPa,“ *International Journal of Engineering Applied Sciences and Technology*, Bd. 3, Nr. 9, pp. 31-36, 2019.
- [11] E. Poursaeidi, A. Moharrami und M. Amini, „Failure Probability and Remaining Life Assessment of Reheater Tubes,“ *JE TRANSACTIONS B: Applications*, Bd. 26, Nr. 5, pp. 543-552, 2013.